RSC Advances

PAPER

View Article Online
View Journal | View Issue

Cite this: *RSC Adv.*, 2017, 7, 14021

Experimental and computational modeling studies on silica-embedded NiO/MgO nanoparticles for adsorptive removal of organic pollutants from wastewater†

Amjad El-Qanni,[ab] Nashaat N. Nassar*[a] and Gerardo Vitale[a]

Achieving affordable and clean water is one of the greatest global challenges of this century. This is due to the enormous upsurge in the world's population, yet at the same time, the scarcity of fresh water. Far more than that, some regions are awash in fresh water while other regions are afflicted by drought. Accordingly, new technological approaches should be brought to the forefront to tackle the water problem. Hence, this study presents three types of newly in-house prepared silica-embedded NiO and/or MgO nanoparticles, namely; SiO_2–NiO, SiO_2–MgO, and SiO_2–$(Ni_{0.5}Mg_{0.5})O$. The properties of these nanoparticles were characterized using XRD, BET, HRTEM, CO_2-TPD, and IR spectroscopy. These nanoparticles are applied for the first time to adsorptive removal of different cationic and anionic model organic molecules with different functionalities, namely: methylene blue (MB), neutral red (NR), and acid red 27 (AR27), mimicking pollutants existing in wastewater effluents. It has been found that on a normalized surface area basis, the number of cationic model molecules adsorbed per nm^2 of the SiO_2–$(Ni_{0.5}Mg_{0.5})O$ nanoparticles were the highest suggesting the possible synergistic effect between Ni and Mg in the mixed oxide, however, SiO_2–NiO showed the highest uptake for the anionic case due to its stability in aqueous solutions. The experimental adsorption isotherms fit well to the Sips model for MB and AR27 indicating a heterogeneous adsorption system. However, a multilayer adsorption behavior was obtained for NR which has been described by the BET model. Computational modeling and DFT calculations of the interaction between the model molecules and the surfaces of the prepared nanoparticles were carried out to get more mechanistic insights into their adsorptive behaviors. The results showed that the adsorbed molecules tend to lie flat on the surface of the materials except for NR which tends to be adsorbed slightly tilted when compared with the others. Additionally, molecular dynamics simulation was performed to gain additional insights into the adsorption behavior of NR in the presence of water. The evolved profile of total energy of the system as a function of simulation time emphasized the eccentric BET adsorption behavior of NR onto these novel nanoparticles.

Received 15th January 2017
Accepted 21st February 2017

DOI: 10.1039/c7ra00615b

rsc.li/rsc-advances

1. Introduction

The arena of water and wastewater treatment is a cutting-edge topic worldwide as water is an essential resource for drinking, daily public use, industrial processes, and medicine.[1] The global water pollution and shortage have been driven by several factors, including: worldwide population growth, competing demands from a variety of users, rapid world industrialization, increasing technical development and living standards, and long-term droughts.[2,3] Therefore, with the ongoing spread of a wide range of industrial pollutants into surface and ground water bodies as well as the water shortage crisis, researchers, engineers, environmentalists, and decision makers are striving to find economically viable alternatives and environmentally sound techniques for water and wastewater treatment processes.[4] Several physical, chemical and biochemical processes have been reported for removing organic-based pollutants from wastewater bodies.[5–7] Typically, these processes are hampered by their ineffectiveness in meeting permissible disposal levels or by their high capital and operating costs. In recent years, nanotechnology, typically in the form of powder nanoparticles or particles integrated with conventional treatment processes, has shown an unprecedented rate in pollution removal and toxicity mitigation.[8–12] The uniqueness of these nanoparticles, especially iron-oxide-based ones, is not only their high surface area, but also

---

[a] Department of Chemical and Petroleum Engineering, University of Calgary, Calgary, Alberta, T2N 1N4, Canada. E-mail: nassar@ucalgary.ca; Fax: +1 403 210 3973; Tel: +1 403 210 9772

[b] Department of Chemical Engineering, An-Najah National University, P.O. Box 7, Nablus, Palestine

† Electronic supplementary information (ESI) available. See DOI: 10.1039/c7ra00615b

properties like magnetism, selective surface reactivity, rapid ion delivery, surface plasmonic resonance, quantum confinement, high adsorption affinity, enhanced catalytic activity, dispersibility, and intrinsic reactivity.[9,13–19] Hence, these nanoparticles were successfully employed as "nanoadsorbents",[16,17,20] "nanocatalysts",[21–23] and recently as "nanosorbcats"[24,25] for cleaning up wastewater. Although a simple search through any scientific search engine with the keywords "nanoadsorbents" and/or "nanocatalysis" would clearly indicate an exponential growth in scientific publications in the past few decades.[23,26] However, the concept of "nanosorbcats" was introduced for the first time by our research group,[24] and has since been tested by other investigators.[25,27,28] It refers to the use of nanoparticles as adsorbent for sequestering the waste organic compounds from wastewater bodies and subsequently as a catalyst for decomposing the adsorbed species into new commodity product. Hence, this allows not only water recyclability and waste hydrocarbons conversion, but also nanosorbcats regeneration. However, to maximize the sustainability of the nanosorbcats, it is important that the developed nanosorbcats be earth abundant, economical and environmentally friendly. Thus, in addition to understanding the adsorption behavior of different organic species, another major purpose of this study is to develop new silica-based nanosorbcats functionalized with active species.

Herein, in continuation of previous work on using nanoparticles as adsorbents and catalysts for waste hydrocarbons, we present novel nanomaterials to improve water recyclability and hydrocarbon conversion. Thus, the purposes of this study include: (1) preparing silica-embedded NiO and/or MgO nanoparticles, which are believed to be efficient nanosorbcats for organic adsorption followed by catalytic steam gasification reaction; (2) comparing the adsorptive performances of the prepared nanosorbcats for the adsorption of different pollutants with different functionalities, like methylene blue (MB), neutral red (NR), and acid red 27 (AR27); and (3) carrying out computational modelling to understand the adsorption mechanism and surface activity of the silica-embedded NiO and/or MgO nanoparticles in order to validate the experimental findings. Experimental adsorption isotherms were described by the Sips and BET models. Worth mentioning here that active nanoparticles, NiO and/or MgO, were embedded in silica to keep them robust and stable for subsequent catalytic steam gasification of the adsorbed species as well as regeneration processes. However, the catalytic activity of the prepared nanosorbcats will be addressed in future publications.

2. Materials and methods

2.1 Chemicals and reagents

In a typical preparation of silica-embedded NiO and/or MgO nanoparticles, the following chemicals and reagents were used; nickel nitrate ($Ni(NO_3)_2 \cdot 6H_2O$ 99.99%), magnesium nitrate ($Mg(NO_3)_2 \cdot 6H_2O$ 99%), ammonium hydroxide (NH_4OH 27% (w/w)), nitric acid (HNO_3 70% (w/w)), Ludox AS-40 colloidal silica (SiO_2 40% (w/w)) purchased from Sigma-Aldrich (Ontario, Canada), silicic acid (H_2SiO_3) powder obtained from Matheson Coleman & Bell (New Jersey, USA), and granulated household sucrose ($C_{12}H_{22}O_{11}$). Potassium bromide (KBr) obtained from Sigma-Aldrich (Ontario, Canada) was used for the infrared analysis. Liquid nitrogen (N_2 99.9% ultrahigh purity) purchased from Praxair (Calgary, Canada) was used for the surface area measurements of the prepared nanoparticles. Gas cylinders of helium (He 99.9% ultrahigh purity) and carbon dioxide (CO_2 99.9% ultrahigh purity) purchased from Praxair (Calgary, Canada) were used for the surface basicity measurements of the prepared nanoparticles. All chemicals were used as received without further purification.

2.2 Adsorbates

Different model molecules with different functionalities and known chemical structures were used as adsorbates in preparing synthetic wastewater samples to understand the adsorption mechanisms; experimentally and computationally. Hence, methylene blue (MB, $C_{16}H_{18}ClN_3S$, $M_w = 374$ g mol^{-1}, $\lambda_{max} = 625$ nm, organics content 82%) and neutral red (NR, $C_{15}H_{17}ClN_4$, $M_w = 289$ g mol^{-1}, $\lambda_{max} = 539$ nm, organics content 90%) were selected as sources of cationic pollutants; while acid red 27 (AR27, $C_{20}H_{11}N_2Na_3O_{10}S_3$, $M_w = 605$ g mol^{-1}, $\lambda_{max} = 520$ nm, organics content 90%) was selected as a source for an anionic pollutant. All model molecules were purchased from Sigma-Aldrich (Ontario, Canada) and used as received without further purification.

2.3 Synthesis of silica-embedded NiO and/or MgO nanoparticles

In brief, silica-embedded NiO (SiO_2–NiO) nanoparticles were prepared by adding 4.3 g of colloidal silica to a 1 L glass beaker containing 200 mL of deionized water. The mixture was agitated using a magnetic stirrer (300 rpm) for 2 min until a homogenous solution was obtained. Then, while keeping the magnetic stirring at 300 rpm, 16.8 g of $Ni(NO_3)_2 \cdot 6H_2O$ was added to the mixture. After complete dissolution of the nickel salt, 13.0 g of granulated household sucrose was added to the mixture. Afterward, 1.5 mL of HNO_3 was added dropwise to the mixture. The mixture was magnetically stirred at 300 rpm and 293 K for 30 min to produce a homogeneous blackish solution. The second type, silica-embedded MgO (SiO_2–MgO) nanoparticles were prepared by adding 4.0 mL of NH_4OH dropwise to another 1 L glass beaker containing 300 mL of deionized water, then, 4.0 g of H_2SiO_3 was added to the mixture and agitated using a magnetic stirrer for 10 min at 300 rpm. After that, 20.0 g of granulated household sucrose and 24.0 g of $Mg(NO_3)_2 \cdot 6H_2O$ were added to the mixture. After complete dissolution of the magnesium salt, 4.0 mL of HNO_3 was added dropwise to the mixture. The mixture was magnetically stirred at 300 rpm and 293 K for 30 min to produce a homogeneous brownish solution. For the sake of studying the possible synergistic effect of bimetallic nanoparticles towards adsorption of cationic and anionic pollutants, silica-embedded NiO and MgO (at a ratio of 0.5 : 0.5) nanoparticles were also prepared in this study. Thus, the third bimetallic type, silica-embedded NiO and MgO (SiO_2–($Ni_{0.5}Mg_{0.5}$)O) nanoparticles were prepared by adding 5.1 g of colloidal silica to a third 1 L beaker containing 225 mL of deionized water. The mixture was agitated using a magnetic stirrer for 2 min until a homogenous solution was obtained. Then, while keeping the magnetic stirring, 9.9 g of $Ni(NO_3)_2 \cdot 6H_2O$ and 9.1 g of $Mg(NO_3)_2 \cdot 6H_2O$ were added to the mixture. After complete dissolution of the nickel and magnesium salts, 15.0 g of granulated household of sucrose and 1.5 mL of HNO_3 were added to the mixture. The mixture was magnetically stirred at 300 rpm and 293 K for 30 min to produce a homogeneous greyish solution. Afterward, all glass beakers were then placed in the oven at 373 K for 48 h to evaporate the water. After 48 h, dried solid materials looking like sponge cakes were obtained. These solid materials were replaced in the oven at 523 K for 12 h. Eventually, all solid materials were taken out, separately, from the oven and then milled in the fume hood until homogeneous powders were obtained and then, calcined in the oven at 1073 K for 3 h in a flow of air and ramping at 5 K min^{-1}. Further details for each nanoparticle's synthesis can be found in the (ESI, Section S1†). In addition, the estimated NiO and MgO content for all prepared nanoparticles can be found in (ESI, Section S2†).

2.4 Characterization of prepared silica-embedded NiO and/or MgO nanoparticles

2.4.1 X-ray diffraction (XRD). Structures and particle crystalline domain sizes of dried silica-embedded NiO and/or MgO nanoparticles were determined by using X-ray Ultima III Multi-Purpose Diffraction System (Rigaku Corp., The Woodlands, TX) with Cu Kα radiation operating at 40 kV and 44 mA with a θ–2θ goniometer. The crystalline domain sizes were measured using the Scherrer equation as implemented in the commercial software JADE[29] by calculating the full width at half-maximum (FWHM) of the peaks and fitting the experimental profile to a pseudo-Voigt profile function.

2.4.2 Textural properties. The surface areas and pore size distributions of the prepared nanoparticles were measured following the Brunauer–Emmett–Teller (BET) and Barrett, Joyner and Halenda (BJH) methods, respectively. These were accomplished by performing N_2 physisorption at 77 K using a surface area and porosity analyzer TriStar II 3020 (Micromeritics Instrument Corporation, Norcross, GA). Test samples were degassed at 423 K under N_2 flow overnight before analysis to remove any existed moisture. Specific surface areas were calculated using BET equation and external surface areas were obtained by the *t*-plot method.

2.4.3 High resolution transmission electron microscopy (HRTEM). Transmission electron microscopy images for silica-embedded NiO and/or MgO nanoparticles were obtained *via* FEI Tecnai F20 FEG TEM using an accelerating voltage of 200 kV to analyze the nanoparticles morphology. This technique provides atomic-resolution real space imaging for nanoparticles. Around 0.5 mg of each test sample was dispersed in 1 mL pure ethanol and stirred for approximately 10 min to ensure that the sample was completely suspended. Then, a drop of the solution was deposited on the sample holder by a pipette. Once ethanol evaporated, the powder was placed on the grid holder and became ready for imaging. An HRTEM carbon grid was used for supporting the sample.

2.4.4 Temperature-programmed desorption of CO_2 (CO_2-TPD). The measurement of surface basic sites on the prepared silica-embedded NiO and/or MgO nanoparticles was carried out by performing CO_2 temperature-programmed desorption (CO_2-TPD) using a CHEMBET 3000 instrument (Quantachrome Inc., USA), equipped with a thermal conductivity detector (TCD). A known amount of each test sample was held in a quartz U-tube. Before starting any measurement, the sample was pretreated on a pretreatment station, to remove air and any physisorbed water by passing He at 473 K for 60 min. After the pretreatment was performed, the U-tube was moved to CHEMBET station set at 373 K with He flow rate of 15 mL min^{-1}. Afterward, CO_2 adsorption was started by passing pure CO_2 through the sample at 373 K for 60 min at a flow rate of 15 mL min^{-1}. After that, CO_2 flow was closed and pure He was passed at 373 K to remove excess/physisorbed CO_2 for 60 min. The temperature was then increased at a heating rate of 10 K min^{-1} to 1223 K, keeping He flowing at 15 mL min^{-1}. CO_2 desorption as a function of temperature was followed by using the TCD, registering the data in the PC-TPRWin program provided with the instrument. The area under the peak was obtained with the PC-TPRW in program and transformed into μmol of CO_2 desorbed per gram of sample (μmol CO_2 per g) using a calibration curve made for this purpose.

2.4.5 Infrared spectroscopy (IR). An IRAffinity-1S instrument (Shimadzu Scientific Instruments Inc., USA) with a smart diffuse reflectance attachment to carry out diffuse reflectance infrared Fourier transform spectroscopy (DRIFTS) analysis was used to study the mid-infrared region before and after adsorption experiments, first, to confirm the silica structure in the prepared silica-embedded NiO and/or MgO nanoparticles, and second, to infer the interactions of model molecules with those nanoparticles. In a typical measurement, around 2.5 mg of the sample was mixed with around 500 mg of KBr and the entire mixture was mounted in the DRIFTS sample holder. Using the associated IRsolution software, the spectra were recorded and analyzed from 400 to 4000 cm^{-1} with a resolution of 4 cm^{-1} and each spectrum was the average of 50 scans.

2.5 Adsorption experiments

Adsorption of model molecules (*i.e.*, MB, NR, and AR27) onto silica-embedded NiO and/or MgO nanoparticles was performed individually at 293 K. Batch adsorption experiments were carried out by adding a specified mass (about 0.10 g) of the silica-embedded NiO and/or MgO nanoparticles to a set of 25 mL vials containing 10 mL of aqueous solutions with initial concentrations ranging from 15 to 1000 μmol L^{-1} of each model molecule at neutral pH of 7.0 ± 0.1. The vials were tightly sealed to avoid any loss of water by evaporation. Adsorption took place by shaking the vials for 24 h on a Wrist Action shaker (Burrel, Model 75-BB) to ensure that the equilibrium was attained. In all experiments, the nanoparticles containing adsorbed model molecules were separated from the mixtures by centrifugation for 10 min at 5000 rpm using an Eppendorf Centrifuge 5804 (Thermo Fisher Scientific Inc., Canada), and the supernatants were decanted. The nanoparticles containing adsorbed model molecules were taken for the IR analysis. The residual concentrations of each model molecule in the supernatants were measured by Evolution™ 260 UV-vis spectrophotometer (Thermo Fisher Scientific Inc., Canada) (UV-vis) at wavelengths of 625, 539, and 520 nm for MB, NR, and AR27, respectively. Pure deionized water identical to that used for preparing model molecules solutions was used as a blank. Calibration curves of UV-vis absorbance at the aforementioned wavelengths against the concentration were first established, using standard solutions with known concentrations of each model molecule. Well fitted regression equations were obtained with linear regression coefficient (R^2) close to unity. Typical standard errors in the model molecules concentration measurements ranged from ±0.5 to 8.0, ±0.7 to 10.4, and ±0.3 to 5.0 μmol L^{-1} for MB, NR, and AR27, respectively. The adsorption uptake per surface area of nanoparticles and nanoparticle adsorption affinity were determined based on the constructed isotherms and mass balance analysis. All experiments were performed in triplicate to confirm reproducibility. The amount adsorbed of each model molecule, Q_e (molecules per nm^2 of nanoparticles), was calculated as shown in eqn (1).[30,31]

$$Q_e = \frac{(C_0 - C_e)N_A}{SA}V \quad (1)$$

where, C_0 is the initial concentration of the model molecule in solution (μmol L^{-1}), C_e is the equilibrium concentration of the model molecule in the supernatant (μmol L^{-1}), V is the solution volume (L), N_A is the Avogadro's constant (molecules per mol), and SA is the BET surface area of the nanoparticles (nm^2).

Macroscopic solution phase adsorption isotherms for MB, NR, and AR27 model molecules were performed to quantify surface coverage onto silica-embedded NiO and MgO nanoparticles. Recently, our research group has concluded that the surface area normalized isotherm data is the best analysis technique for developing a mechanistic interpretation for any model molecule adsorption onto nanoparticles surfaces.[30,31] Thus, our adsorption results were presented on a normalized BET surface area basis (molecules per nm^2). To further understand the adsorption behaviour, the experimental isotherm data were fitted to the Sips model,[32,33] also known as "Langmuir–Freundlich" isotherm,[33] and the BET model[34] expressed by eqn (2) and (3), respectively.

$$Q_e = \frac{Q_m K_s {C_e}^{n_s}}{1 + K_s {C_e}^{n_s}} \quad (2)$$

$$Q_e = Q_m \frac{K_L C_e}{(1 - K_U C_e)(1 - K_U C_e + K_L C_e)} \quad (3)$$

where, Q_e is the equilibrium uptake, *i.e.*, the number of molecules of MB, NR, and AR27 adsorbed per surface area of the dried nanoparticles (molecules per nm^2), C_e is the equilibrium concentration of each model molecule in the supernatant (μmol L^{-1}), Q_m is the maximum adsorption capacity for complete monolayer coverage (molecules per nm^2), K_s is the equilibrium constant of adsorption related to the adsorption affinity (L μmol^{-1})^{n_s}, n_s is the Sips constant related to the surface heterogeneity (unitless), and K_L (L nm^{-2}) and K_U (L nm^{-2}), are the equilibrium constants of adsorption for the lower and the upper layers, respectively. The non-linear chi-square (χ^2) analyses[35] were used to evaluate the goodness of fitting as per eqn (4)

$$\chi^2 = \sum \frac{(Q_e - Q_{emodel})^2}{Q_{emodel}} \quad (4)$$

where, Q_e and Q_{emodel} are the equilibrium uptake of each model molecule obtained experimentally and by model fitting, respectively. The lower the value of χ^2 the better the fitting. All isotherm model parameters and the χ^2 analyses were performed using OriginPro 8 SR4 software (Version 8.0951).

2.6 Computational modeling

Computational modeling was carried out to get some insights into the adsorption interactions of AR27, MB and NR molecules with the surfaces of NiO, MgO and amorphous silica nanoparticles. NiO and MgO have the rocksalt structure (similar to many other binary oxides) and our interest in them is going to be focused on their surface interactions with three model molecules (AR27, MB, and NR). Starting from the experimental structural data within BIOVIA Material Studio 2017 (MS2017) database,[36] we created two low index surfaces, the (100) and (111), for each oxide (*i.e.*, NiO and MgO) and also an amorphous silica surface was created to carry out our studies of AR27, MB and NR interactions with these selected surfaces. The solid-solution ($Ni_{0.5}Mg_{0.5}$)O was not studied because producing a single accurate structural model for this case requires the generation of supercells, where several Ni and Mg atom configurations within the supercell can be generated, which in turn will produce many feasible mixed ($Ni_{0.5}Mg_{0.5}$)O models complicating the selection of a single model for the calculations. Also, the lack of accuracy might occur by using mixed forcefields for the oxygen atoms present in the solid crystalline supercell containing Mg and Ni atoms at the same time. For this part of the computational studies, we used the modules Forcite and Adsorption Locator included within the commercial modeling software MS2017.[36] BIOVIA Forcite is an advanced classical molecular mechanics tool, designed to work with a wide range of forcefields, allowing fast energy calculations and reliable geometry optimizations of molecules and periodic systems. In our study, Forcite was used to geometrically optimize the AR27, MB, NR and H_2O molecules, to optimize the NiO, MgO and amorphous silica unit cells and to relax the surface atoms of the created low index surfaces prior to their use in the adsorption study. For the latter task, we used BIOVIA Adsorption Location module which is based on simulated annealing (a metaheuristic algorithm for locating a good approximation to the global minimum of a given function in a large search space[37,38]) allowing in this way identification of the possible adsorption configurations by carrying out Monte Carlo searches of the configurational space of the selected surfaces-model molecules systems as the temperature is slowly decreased. In order to identify additional local energy minima, the process is repeated several times.

Atomistic simulations of inorganic–organic interfaces require an accurate description of interatomic forces, and thus, for the present study we employed BIOVIA COMPASSII forcefield as it can simulate not only organic molecules but also bulk metal oxides as well as interactions between them.[36,39] The Condensed-phase Optimized Molecular Potentials for Atomistic Simulation Studies (COMPASS) is the first *ab initio* forcefield that has been parametrized and validated using condensed-phase properties in addition to various *ab initio* and empirical data for molecules in isolation. Consequently, this forcefield enables accurate and simultaneous prediction of structural, conformational, vibrational, and thermophysical properties that exist for a broad range of molecules in isolation and in condensed phases including interfaces and mixtures.[39–45] Currently, the coverage of this forcefield includes the most common organics, inorganic small molecules, polymers, some metal ions, metal oxides, and metals.[36] The following subsections show the details of the theoretical calculations.

2.6.1 AR27, MB, NR, and H_2O molecules. The AR27, MB, NR and H_2O molecules were built and optimized with BIOVIA Forcite before adsorbing them onto the selected surfaces. The quality of the Geometry Optimization in BIOVIA Forcite was set to Fine and the Forcefield to BIOVIA COMPASSII, as this forcefield is compatible with metal oxides,[37] and will be used to study the interactions of these molecules with the metal oxide surfaces. The optimized AR27, MB and NR molecules are presented in Fig. 1, where an almost flat configuration of the molecules can be observed.

2.6.2 NiO and MgO surfaces. The experimental structural data for NiO and MgO reported in the MS2017 structural database[36] was transferred and the unit cells were geometrically optimized within BIOVIA Forcite. The quality of the Geometry Optimization in BIOVIA Forcite was set to fine and the forcefield to BIOVIA COMPASSII, as this forcefield is compatible with organic molecules, and thus, suitable for studying the interactions of these organic molecules with the oxide surfaces.[39] The experimental unit cell values for NiO and MgO, reported in the MS2017 structural database,[36] are 0.41684 nm and 0.42112 nm, respectively, and the optimized unit cell values obtained with Forcite and the COMPASSII forcefield were 0.41683 nm for NiO and 0.42318 for MgO, which are very similar to the experimental ones; indicating and confirming the employed quality of the forcefield. The amorphous silica model within BIOVIA structural database was also optimized with Forcite using the COMPASSII forcefield. These optimized unit cells were then used within BIOVIA Builder module to create the surfaces (100) and (111) for each oxide and (100) for the amorphous silica. Each surface was created with areas of approximately 9 nm^2 ($\sim$3 nm × $\sim$3 nm) to ensure that the selected molecules do not interact with their images in adjacent cells. The depth of the surfaces was set to approximately 2.0 nm to ensure that it was greater than the non-bond cutoff used in the calculation. The vacuum thickness was set to 4 nm so the organic molecules do not interact with the periodic image of the bottom layer of atoms in the surface. The internal coordinate atoms in these surfaces were fixed to their bulk values and the top layers of atoms ($\sim$0.5 nm) which will interact with the organic molecules were allowed to relax under the geometric optimization carried out with BIOVIA Forcite with the BIOVIA COMPASSII forcefield that has been parametrized for metal oxides, and is suitable to study interactions between organics and inorganics.[36,39]

2.6.3 Interaction of AR27, MB, NR and H_2O molecules with NiO and MgO surfaces. BIOVIA Adsorption locator module was used to gain insights into the interactions of the selected molecules with the produced surfaces. The simulating annealing task in BIOVIA Adsorption Locator calculation was set to a quality of Fine (energy cutoff of 1.0×10^{-4} kcal mol^{-1}) using the Smart algorithm. The atom based summation method was used for van der Waals and the group based method for the electrostatic with a cubic spline truncation and a cutoff distance of 1.55 nm. The forcefield selected was BIOVIA COMPASSII, which is suitable to study interfaces between organics and inorganics,[36,39] the top layer atoms ($\sim$0.5 nm) on the different surfaces were selected for the interaction with AR27, MB, NR and H_2O molecules, and the maximum adsorption distance value was 1.5 nm with a fixed energy window of 10 kcal mol^{-1} for sampling configurations which differ from the lowest configuration in that maximum amount. Also, a combination of one NR molecule with 100 H_2O molecules was carried out to understand the effect of water on the adsorption.

2.6.4 DFT calculations for the AR27, MB and NR molecules. To gain further comprehension of the studied model

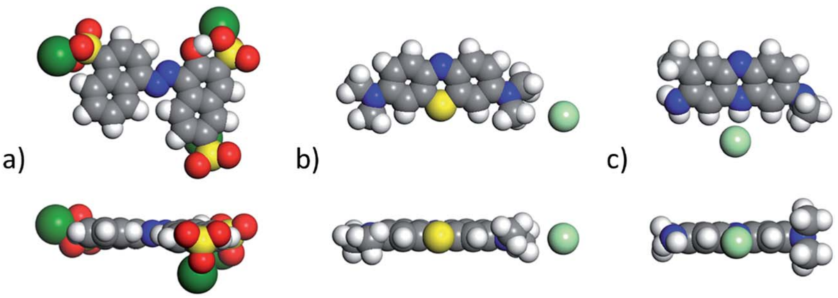

Fig. 1 CPK representation of the optimized molecules showing its optimized configuration (top and side views, respectively). (a) AR27, (b) MB, and (c) NR. Grey atoms represent carbon, blue atoms represent nitrogen, white atoms represent hydrogen, yellow atoms represent sulfur, dark green atoms represent sodium, pale green atoms represent chlorine and red atoms represent oxygen.

molecules in the employed aqueous systems, the electronic structure of the AR27 anion, MB and NR cations, and water molecules as well as Na^+ and Cl^- counterions was obtained at the DFT level using DMOL3 and the meta-GGA M06-L functional with the DNP+ numerical basis set applying the COSMO solvation model (conductor-like screening model),[46] where the aqueous solvent was represented by the dielectric constant of water ($\varepsilon = 78.54$). The following convergence tolerances were applied: energy = 1.0×10^{-5} Ha; max. force = 0.002 Ha Å^{-1}; max. displacement 0.005 Å; using a smearing of 0.005 Ha and a Global orbital cutoff of 5.0 Å. Atomic charge distribution was obtained through Hirshfeld population analysis.[47]

2.6.5 Molecular dynamics simulations. In order to gain additional insights into the adsorption behavior of NR in the presence of water, molecular dynamics (MD) simulations were performed using the Forcite module within BIOVIA MS2017 software.[36] The interatomic interactions were described by using the COMPASII forcefield.[39] The MD simulations were conducted in NVT ensemble at 298 K. The Nosé method[48] was employed in the thermostat to control the thermodynamic temperature with a Q ratio of 0.01. The time step in the MD simulation was set to 0.5 fs, and the data were collected every 1 ps. The simulation time was set to 1 ns to detect several cycles of thermal vibration, and the full-precision trajectory was recorded. Energies and other statistical data (coordinates, velocities, *etc.*) were stored every 5000 steps during the simulations.

For the simulation, the system was defined as a periodic slab with the (100) face because it is the most probable exposed surface on the MgO or NiO materials. The dimensions of the surface were similar to those used in the Adsorption Locator calculations (*i.e.* ∼3 nm × ∼3 nm). The thickness of the slab was set to ∼2 nm and the three upper layers of atoms were allowed to freely evolve without any geometrical constraints during the calculations. The rest of the atoms were fixed to the geometrically optimized values in the bulk. A vacuum of 23 nm was imposed on top of the oxide surface and a slab of about 2.5 nm containing 500 water molecules and 5 NR molecules, generated by the BIOVIA Amorphous Cell module and the COMPASII forcefield, was added close to the oxide surface within the periodic cell.

3. Results and discussions

3.1 Characterization studies

3.1.1 XRD of silica-embedded NiO and/or MgO nanoparticles. XRD patterns of the prepared nanoparticles are shown in Fig. 2. The sharp peaks in the XRD patterns imply good crystallinity for all the crystalline metal-oxide products. The identification of the patterns confirms the material to be bunsenite, periclase, and the combination of both materials for SiO_2–NiO, SiO_2–MgO, and SiO_2–$(Ni_{0.5}Mg_{0.5})O$ nanoparticles, respectively. It is worth noting here that there are small series of peaks below 30 degrees refer to some traces of forsterite (Mg_2SiO_4) in the case of SiO_2–$(Ni_{0.5}Mg_{0.5})O$ nanoparticles (Fig. 2). The structures were identified by comparing the XRD signals with those reported in the pdf cards 01-075-0269 (bunsenite), 01-077-2364 (periclase), and 00-007-0074 (forsterite) of the 2005 International Centre for Diffraction Data (ICDD) database included in the program JADE V.7.5.1 (Materials Data XRD Pattern Processing Identification & Quantification).[29] As seen in Fig. 2, the peaks are broad indicating that the prepared silica-embedded NiO and/or MgO nanoparticles have indeed small crystalline domain sizes; 21, 23, and 12 nm for SiO_2–NiO, SiO_2–MgO, and SiO_2–$(Ni_{0.5}Mg_{0.5})O$ nanoparticles, respectively. This was expected due to the atomic arrangements after the calcination process (1073 K for 3 h) during the synthesis which allowed the atomic amorphous material to get closer and produce nanoparticles with around 25 nm crystalline domain sizes for NiO and MgO nanoparticles. Also, it is noteworthy mentioning that the particle size of colloidal silica was in the range of 20.0–24.0 nm as reported by the manufacturer (Sigma-Aldrich). However, upon adding them to the water solution the size increased to 45 nm due to the loss of ionic strength, as detected by the Malvern NanoSight (NS300, Massachusetts, US) instrument and analyzed by the nanoparticle tracking analysis

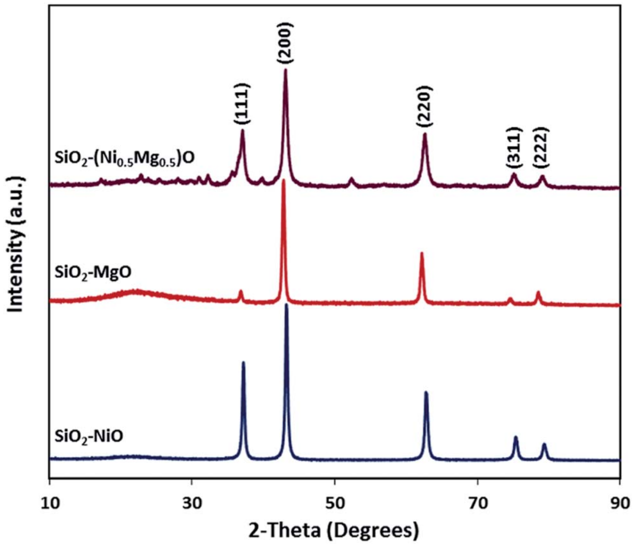

Fig. 2 X-ray diffraction powder patterns, with the respective Miller index for each one of the reflections of the cubic structure, of the prepared silica-embedded NiO and/or MgO nanoparticles.

Table 1 BET surface areas of silica-embedded NiO and MgO nanoparticles

Measurement	SiO_2–NiO	SiO_2–MgO	SiO_2–$(Ni_{0.5}Mg_{0.5})O$
BET specific surface area ($m^2\ g^{-1}$)	56	98	44
External surface area, *t*-plot ($m^2\ g^{-1}$)	52	89	40
Micropore area, *t*-plot ($m^2\ g^{-1}$)	4	9	4
Pore width (nm), BJH analysis	15	3.5	9
Pore volume × 10^2 ($cm^3\ g^{-1}$), BJH analysis	42	52	25

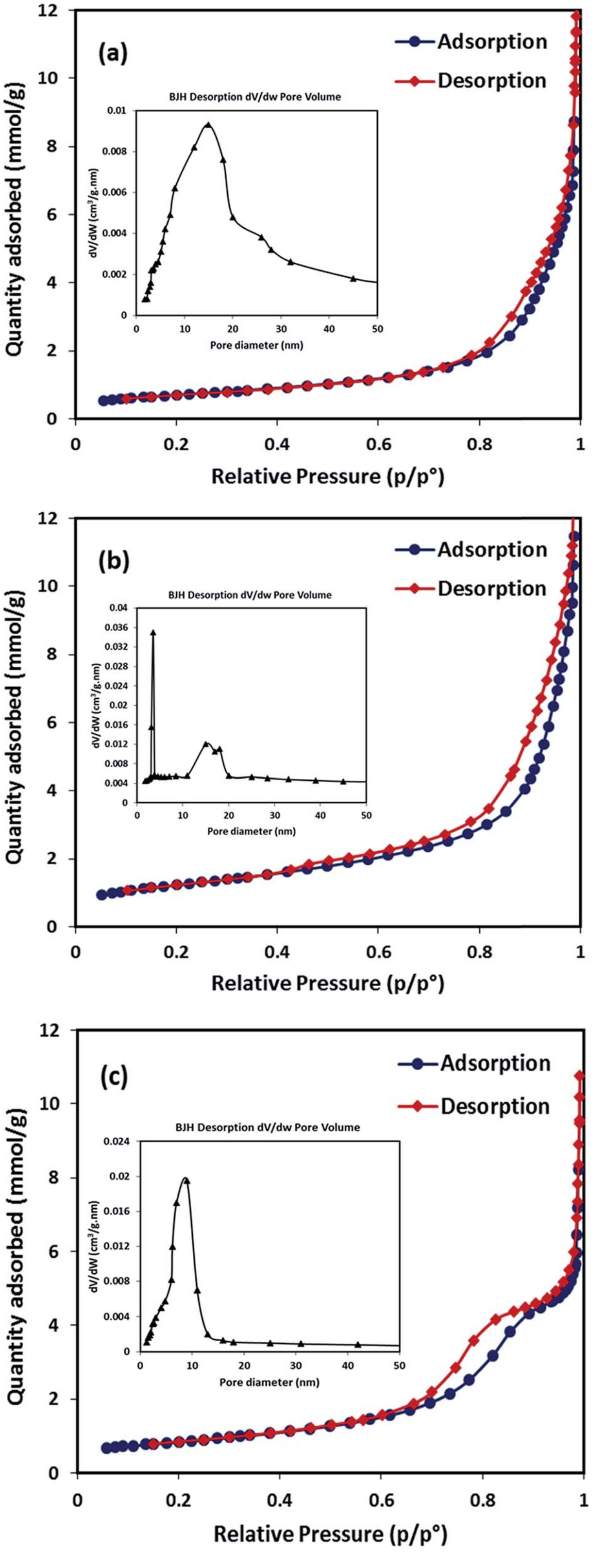

Fig. 3 Nitrogen physisorption isotherms for (a) SiO_2–NiO, (b) SiO_2–MgO, and (c) SiO_2–$(Ni_{0.5}Mg_{0.5})O$ nanoparticles.

(NTA) software. This particle size range could play a role on the produced crystalline domain sizes, especially for NiO and MgO nanoparticles. The crystalline domain size is the lowest for SiO_2–$(Ni_{0.5}Mg_{0.5})O$ nanoparticles. This could be attributed to the bimetallic interaction between the solid solution of MgO and NiO affecting somehow the growth of its crystalline domain size up to 12 nm. Also, it may be possible that the traces of the forsterite crystalline phase may be playing a disrupting role for the growth of the Ni–Mg mixed oxides nanocrystalline domains.

3.1.2 Textural properties. The textural properties values of external and internal surface areas, as well as pore size distributions of the prepared silica-embedded NiO and/or MgO nanoparticles, are shown in Table 1. Fig. 3 shows the N_2 physisorption isotherms together with the pore size distributions of these nanoparticles. As seen in Table 1, no significant differences were observed between the surface areas obtained by the BET and *t*-plot methods for the prepared silica-embedded NiO and/or MgO nanoparticles. However, the results of the BJH analysis show pore widths of 15, 3, and 9 nm for SiO_2–NiO, SiO_2–MgO, and SiO_2–$(Ni_{0.5}Mg_{0.5})O$ nanoparticles, respectively, which falls into the mesoporous scale (2–50 nm) as classified by the International Union for Pure and Applied Chemistry (IUPAC).[49,50] Moreover, IUPAC has classified the physisorption isotherms into six categories (Types I to VI) and the possible hysteresis loops in these isotherms into five categories (Types H1 to H5).[50] Accordingly, the Type II isotherm seems a descriptive isotherm in the case of our prepared nanoparticles as presented in Fig. 3. It is well known in the literature that most metal-oxide-based nanoparticles, including NiO and MgO, are non-porous materials.[24,30,51] However, the presence of mesoporosity and hysteresis loop (Fig. 3) can be attributed to the calcination process during the synthesis of silica-embedded NiO and/or MgO nanoparticles. When the precursor of the nanoparticles was calcined at 1073 K for 3 h, the amorphous carbonaceous part coming from the sucrose was oxidized, and thus, CO_2 was produced and leaned the structure causing some mesoporous channels. Therefore, the expected isotherm should be the pure reversible Type II isotherm without hysteresis that is obtained with non-porous adsorbents. However, our materials showed adsorption isotherms of Type II with hysteresis loops of Type H3. According to IUPAC classification, there are two distinctive features of the Type H3 loop that are: (i) the adsorption branch resembles a Type II isotherm and (ii) the lower limit of the desorption branch is normally located at the cavitation-induced p/p^o. Loops of this type are given by non-rigid aggregates of plate-like particles (as shown in the HRTEM images discussed in Section 3.1.3), also the pore network consists of macropores which are not completely filled with pore condensate. This concludes that the as prepared silica-embedded NiO and/or MgO nanoparticles have no significant porosity and maintain high external surface areas.

3.1.3 Morphology of silica-embedded NiO and/or MgO nanoparticles. To gain further insights into the morphology of the prepared silica-embedded NiO and/or MgO nanoparticles, HRTEM and selected area electron diffraction (SAED) images were taken for selected samples as shown in Fig. 4. HRTEM images confirm the presence of nano-sized particles as indicated by the black spots in Fig. 4(a and b), (d and e), and (g and h) for SiO_2–NiO, SiO_2–MgO, and SiO_2–$(Ni_{0.5}Mg_{0.5})O$ nanoparticles, respectively. Most of the nanoparticles are aggregates of plate-like morphology; justifying the presence of Type H3

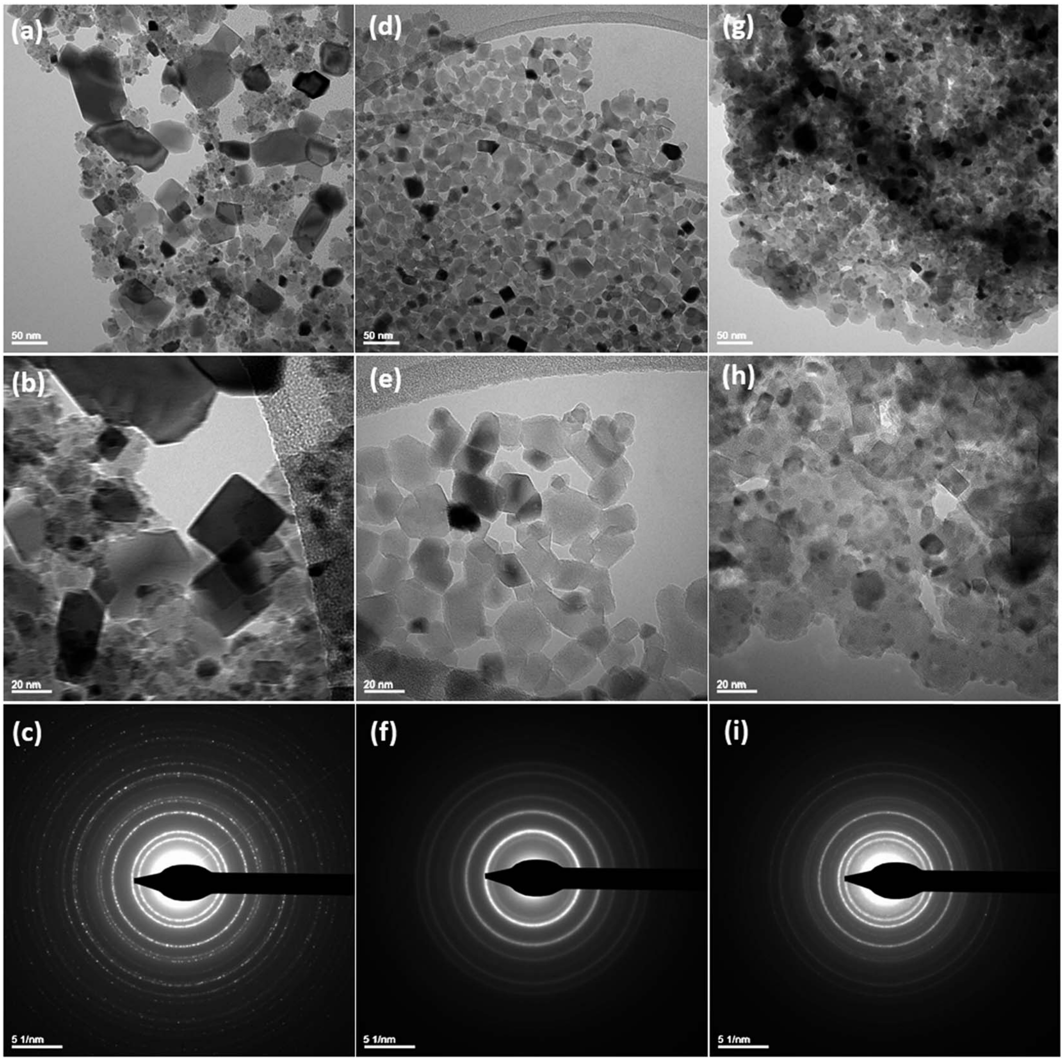

Fig. 4 High resolution transmission electron microscopy and selected area electron diffraction images for (a–c) SiO_2–NiO, (d–f) SiO_2–MgO, and (g–i) SiO_2–$(Ni_{0.5}Mg_{0.5})O$ nanoparticles. Line marks in the images correspond to 50 and 20 nm for images (a, d, g) and (b, e, h), respectively, and 5 nm^{-1} for the SAED images.

hysteresis loops as indicated in Section 3.1.2. Moreover, the SAED pattern of these nanoparticles indicates that they are composed of small crystalline domain sizes as these solids produce circular electron diffraction halos. This indeed lines up with what we observed with the XRD results and agrees with some recent studies found in the literature.[30,52] Tables 2 and 3 show the *d*-spacings obtained from the SAED and their comparisons with the reported and experimental XRD *d*-spacings. As can be seen, the experimentally obtained values (SAED and XRD) agreed well with each other. When compared with the reported values for bulk MgO and NiO it can be noticed that most of the experimental values are slightly higher than the reported ones. However, it has been reported that nanoparticles tend to have larger unit cells when compared to bulk materials as the surface imperfection increases with decreasing the crystalline size affecting the unit cell (*i.e.*, surface/volume ratio of imperfections changes by decreasing the crystalline size).[30,53,54]

3.1.4 CO_2-TPD of silica-embedded NiO and/or MgO nanoparticles. CO_2-TPD experiments were carried out to quantify the amount and to know the relative strength of the basic sites present on the prepared nanoparticles. The results of TPD profiles after CO_2 adsorption on silica-embedded NiO and/or MgO nanoparticles (Fig. 5) together with the results demonstrated in Table 4 confirm that the prepared nanoparticles have different surface basicities. The higher the amount of CO_2 desorbed the higher will be the basicity. As expected SiO_2–MgO has the highest amount of CO_2 desorbed emphasizing their highest basicity, followed by SiO_2–$(Mg_{0.5}Ni_{0.5})O$ and then SiO_2–NiO nanoparticles. Moreover, SiO_2–MgO nanoparticles show a T_{max} for CO_2 desorption around 688 K, while SiO_2–NiO and SiO_2–$(Mg_{0.5}Ni_{0.5})O$ nanoparticles show CO_2 desorption at T_{max} around 490 K. This suggests that SiO_2–MgO nanoparticles when present alone has sites that are very basic in nature as compared to SiO_2–NiO and SiO_2–$(Mg_{0.5}Ni_{0.5})O$ nanoparticles.

Table 2 *d*-Spacings obtained from SAED and their comparisons with the reported and experimental XRD *d*-spacings for the MgO in the SiO_2–MgO sample

	MgO	SiO_2–MgO	
Miller planes	Reported XRD *d* [Å]	Experimental by XRD *d* [Å]	Experimental by SAED *d* [Å]
(1 1 1)	2.4220	2.4401	2.4376
(2 0 0)	2.0975	2.1117	2.1016
(2 2 0)	1.4832	1.4919	1.4975
(2 2 2)	1.2110	1.2177	1.2132
(4 0 0)	1.0488	—	1.0578
(3 3 1)	0.9624	—	0.9576
(4 2 2)	0.8567	—	0.8658

The low basicity found for the SiO_2–$(Mg_{0.5}Ni_{0.5})O$ nanoparticles seems to indicate two possibilities: first, Ni atoms were more exposed on the surface than the Mg atoms in the prepared solid-mixture NiO–MgO, and thus, less strong basic sites for CO_2 adsorption. Second, the presence of Ni affected not only the basic properties of Mg in the mixture of NiO–MgO; but also the total surface area as was experimentally observed and described in Section 3.1.2, and thus, less basic sites for adsorption. Interestingly, the combination of Ni and Mg in the preparation of SiO_2–$(Mg_{0.5}Ni_{0.5})O$ nanoparticles produced a material with half of the crystalline domain sizes of SiO_2–NiO and SiO_2–MgO. Additionally, embedding the bimetallic nanoparticles in the silica may have caused less surface area, and thus, reducing the basic sites for CO_2 adsorption.

3.1.5 IR analysis. The infrared spectra of the prepared silica-embedded NiO and/or MgO nanoparticles are shown in Fig. 6. Clearly, all spectra share similar signals as they all consist of the main framework component; silica structure. Noticeable IR signals at 3700–3420 cm^{-1} are assigned to the –OH stretching vibrations. While a clear, broad IR bands with different intensities centered at around 1600–1345 cm^{-1} that should be assigned to –OH bending vibration modes.[30] The strong and broad IR bands at 1114–1045 cm^{-1} are usually assigned to the Si–O–Si asymmetric stretching vibrations.[55] Furthermore, the IR stretching band at 965 cm^{-1} could be assigned to the silanol groups (Si–OH).[55] The IR signals at 800 cm^{-1} are assigned to Si–O bending vibrations while the Si–O out of plane deformation appears at 450 cm^{-1}.[56] Indeed, our spectra are in good agreement with other silica spectra found elsewhere.[55,57] Moreover, it is well known in the literature that metal-oxide-based materials produce IR bands between 400–1000 cm^{-1} due to the inter-atomic vibrations.[58,59] Thus, the IR signals at 465 and 415 cm^{-1} are assigned to NiO and MgO, respectively. This agrees perfectly with other NiO and MgO IR bands reported in the literature.[30,58–60] With this info at hands we confirm the successful preparation of silica embedded NiO and/or MgO nanoparticles. The previous XRD results (Fig. 2) confirmed the existence of NiO and MgO nanoparticles and they are indeed embedded, as seen previously in the HRTEM images (Fig. 4), into the amorphous silica structure (Fig. 6).

Table 3 *d*-Spacings obtained from SAED and their comparisons with the reported and experimental XRD d-spacings for the NiO in the SiO_2–NiO sample

	NiO	SiO_2–NiO	
Miller planes	Reported XRD *d* [Å]	Experimental by XRD *d* [Å]	Experimental by SAED *d* [Å]
(1 1 1)	2.4111	2.4166	2.4188
(2 0 0)	2.0881	2.0920	2.0943
(2 2 0)	1.4765	1.4786	1.4845
(3 1 1)	1.2592	1.2607	1.2666
(2 2 2)	1.2056	1.2071	1.2071
(4 0 0)	1.0441	—	1.0532
(3 3 1)	0.9581	—	0.9509
(4 2 2)	0.8525	—	0.8636

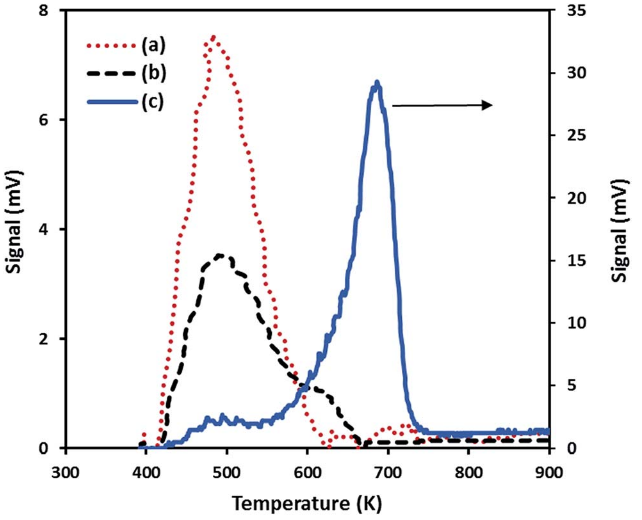

Fig. 5 CO_2 temperature-programmed desorption profiles for (a) SiO_2–NiO, (b) SiO_2–$(Mg_{0.5}Ni_{0.5})O$, and (c) SiO_2–MgO nanoparticles. Experimental conditions: heating rate, 10 K min^{-1}; maximum temperature, 1223 K; He flow rate, 15 mL min^{-1}; the amount of SiO_2–MgO, SiO_2–NiO, and SiO_2–$(Mg_{0.5}Ni_{0.5})O$ nanoparticle were 0.104, 0.403, and 0.195 g, respectively.

3.2 Adsorption isotherms

Fig. 7 shows the experimental isotherm data obtained together with the fit of the Sips and BET models for MB, NR, and AR27 model molecules onto silica-embedded NiO and/or MgO nanoparticles at a temperature of 293 K. The estimated parameters of the Sips and BET models are listed in Table 5. As seen in Fig. 7, a good agreement was achieved between the

Table 4 CO_2-TPD analysis of the prepared silica-embedded NiO and MgO nanoparticles

Nanoparticles	CO_2 uptake (μmol g^{-1})	T_{max} (K)
SiO_2–NiO	90	484
SiO_2–MgO	1148	688
SiO_2–$(Mg_{0.5}Ni_{0.5})O$	130	490

experimental data and the Sips and BET isotherm models, this was also indicated by the low values of χ^2 as shown in Table 5. Clearly, all silica-embedded NiO and/or MgO nanoparticles succeeded in removing MB (Fig. 7a). The adsorption of MB increased sharply at low equilibrium concentration and further gradually increased at high concentration, suggesting that silica-embedded NiO and/or MgO nanoparticles have a high adsorption affinity for MB even at low concentration. This was also indicated by the closeness in K_s values (Table 5). Worth mentioning here that there was a clear observation on color change, the blue color of MB before adsorption became almost colorless after adsorption. As seen, when uptake normalized to BET surface area, there are significant differences in the adsorption of MB molecule onto silica-embedded NiO and MgO nanoparticles. The bimetallic SiO_2–$(Mg_{0.5}Ni_{0.5})O$ nanoparticles were the best adsorbents towards MB adsorption (Fig. 7a), this could be attributed to the possible synergistic effect which may have enhanced the adsorption selectivity towards MB heteroatoms, mainly nitrogen atoms, followed by SiO_2–NiO and then SiO_2–MgO nanoparticles. These findings were also confirmed by the Q_m values (Table 5) estimated from the Sips model. In fact, such synergistic findings agree well with many publications in literature. For instance, Nassar and co-authors,[61–63] investigated the synergistic effect of in-house prepared NiO and PdO nanosorbcats supported on either fumed silica, titanium, or alumina towards asphaltenes adsorption followed by oxidation and/or steam gasification processes. In the adsorption part, the authors noticed that bimetallic nanosorbcats showed higher uptake than monometallic ones which was attributed to the synergistic effect of PdO and NiO that led to different unified selectivities towards the heteroatoms of asphaltene molecules.[61] Li *et al.*,[64] reviewed many rational design of nanomaterials for water treatment, the authors indicated that the synergistically multi-functionalized nanomaterials would pave the way for new

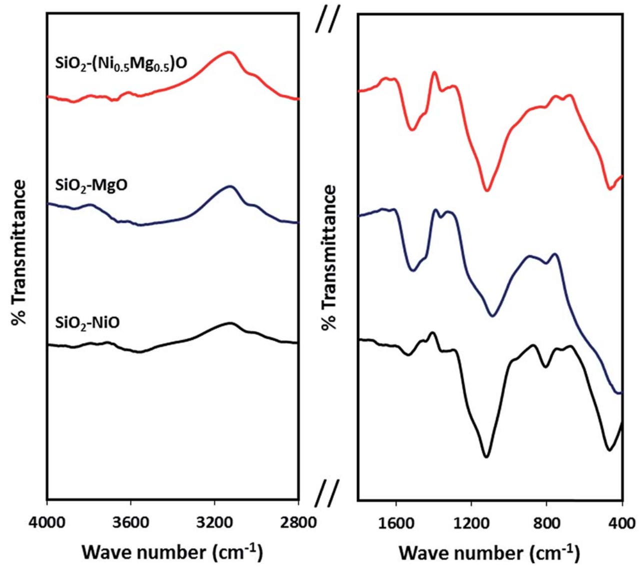

Fig. 6 Infrared spectra of the prepared silica-embedded NiO and/or MgO nanoparticles.

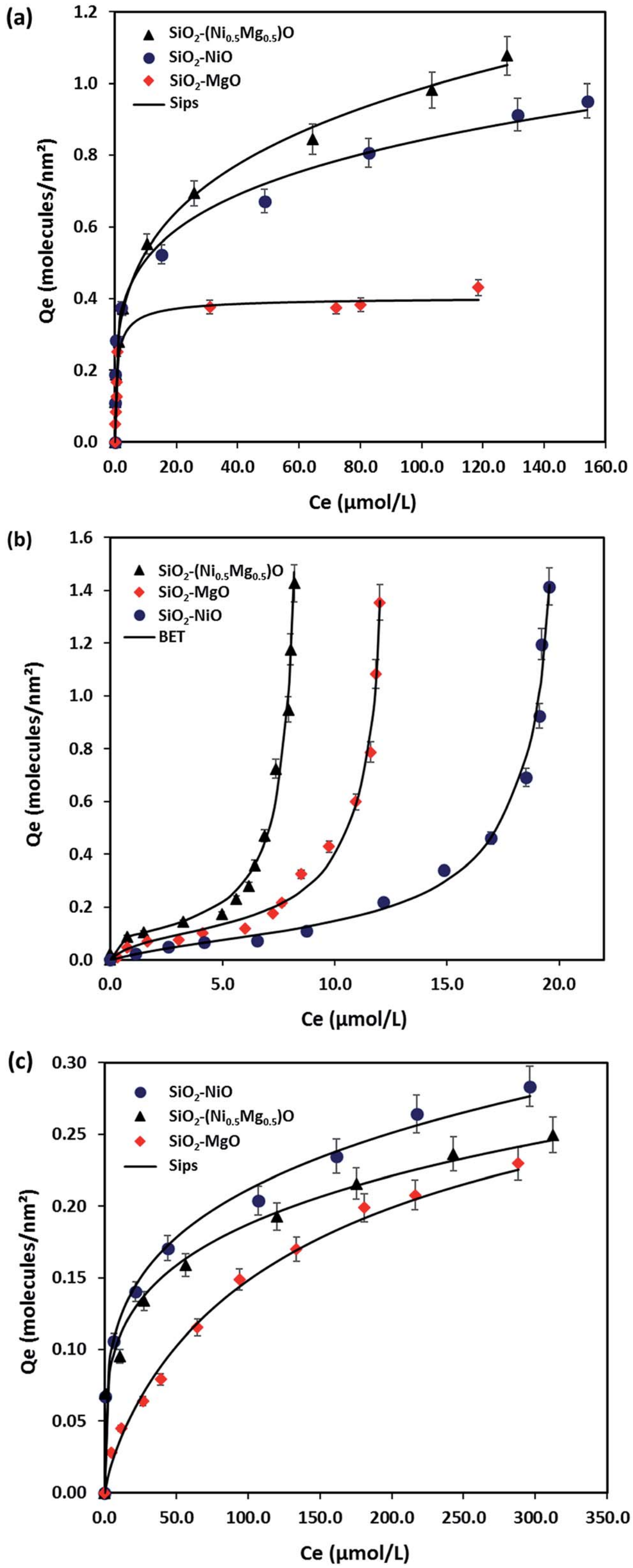

Fig. 7 Macroscopic solution phase adsorption isotherms of (a) MB, (b) NR, and (c) AR27. Experimental conditions are: nanoparticles dose, 10 g L^{-1}; shaking rate, 200 rpm; contact time, 24 h; and temperature, 293 K; pH, 7.0. The symbols are experimental data, and the solid lines are the Sips and the BET models (eqn (2) and (3)).

adsorption applications that could be easily integrated with the current conventional water and wastewater treatment systems.[65] There are many other investigations on the synergistic effect of graphene and metal-oxide-based adsorbents for organics and dyes removal[66–68] which underpin our findings. One more thing that is important to look at is the n_s values (Sips heterogeneity factor). The Sips isotherm model is used to predict the adsorption on heterogeneous system circumventing the limitation of the rising adsorbate concentration associated with Freundlich isotherm model.[31,69] Thus, the value of n_s in the Sips model plays a major role in determining the interaction type between MB and the surface of silica-embedded NiO and/or MgO nanoparticles. It is related to the existence of lateral interactions between adsorbed molecules which is not considered in the Langmuir theory.[31,70] Table 5 shows the n_s values of less than 0.5 for SiO_2–NiO and SiO_2–$(Mg_{0.5}Ni_{0.5})O$ nanoparticles. This suggests that these nanoparticles may have heterogeneous surfaces with adsorption sites that have different adsorption energies. While the n_s value of SiO_2–MgO nanoparticles is close to one, this suggests that these nanoparticles portray saturation surface coverage and have more homogenous surface.

Fig. 7b shows the experimental isotherm data obtained together with the fit of the BET model for NR molecule adsorption onto the silica-embedded NiO and/or MgO nanoparticles at a temperature of 293 K. An excellent agreement between the experimental data and the BET model is seen in Fig. 7b and indicated by the low values of χ^2 (Table 5). Although, NR was used as another cationic pollutant in this study, an eccentric type of adsorption was noticed in comparison with the MB. The adsorbed amount of NR molecules increased exponentially with the equilibrium concentration. The BET model describes the multilayer adsorption phenomena for gas–solid and liquid–solid equilibrium systems.[71–73] Such adsorption isotherm characterizes the multilayer adsorption on non-porous solids with weak adsorbent–adsorbate interactions.[73,74] Nassar *et al.*,[73] and Franco *et al.*,[74] indicated that with such adsorption behavior the interaction between an adsorbate (*i.e.*, NR in this case) and an adsorbed layer is greater than the interaction with the adsorbent surface (*i.e.*, silica-embedded NiO and MgO nanoparticles) where adsorption increases exponentially. As seen in Fig. 7b, SiO_2–$(Mg_{0.5}Ni_{0.5})O$ nanoparticles seem again to be the best adsorbents for the second cationic pollutant (NR), this was also indicated by the highest estimated BET constants shown in Table 5, which confirms their possible synergistic effect. Surprisingly, SiO_2–MgO nanoparticles seem to be the best adsorbents towards NR than SiO_2–NiO nanoparticles. A reasonable explanation for this could be linked to the absence of C–S bonds in the NR structure, which enabled a better interaction and adsorption affinity between the first layer of adsorbed NR onto SiO_2–MgO nanoparticles. This was also indicated by the K_L values shown in Table 5. Similar adsorption trends and behaviors of different types of pollutants, including; dyes, phenols, and olive mill wastewaters, can be found elsewhere.[72,73,75,76]

Fig. 7c shows the adsorption of an anionic pollutant source (AR27) onto silica-embedded NiO and/or MgO nanoparticles. Clearly, the adsorption affinities of SiO_2–NiO and SiO_2–$(Mg_{0.5}Ni_{0.5})O$ nanoparticles are higher than the SiO_2–MgO nanoparticles, as seen in Fig. 7c and indicated by the K_s values (Table 5). As seen in Fig. 7c, SiO_2–NiO nanoparticles appear to be the best adsorbents towards AR27 adsorption as also indicated by its highest Q_m values (Table 5). This could be attributed to the heterogeneity of the nanoparticles surface as they appear to have the lowest value of n_s, which implies that these nanoparticles surface are heterogenous with adsorption sites that have different adsorption energies. Although, the order of SiO_2–$(Mg_{0.5}Ni_{0.5})O$ nanoparticles comes to the second place, but apparently, the synergistic effect made its adsorptive behavior towards AR27 better than SiO_2–MgO nanoparticles. This was also indicated by the estimated Sips model constants shown in Table 5. Recalling the CO_2-TPD results shown previously in Section 3.1.3, we proposed that Ni atoms were more exposed on

Table 5 Estimated Sips and BET isotherm constants for the adsorption of the model molecules (dyes) over silica-embedded NiO and MgO nanoparticles at a temperature of 293 K

		Sips model parameters			
Model molecule	Nanoparticles	K_s (L μmol^{-1})^{n_s}	Q_m (molecules per nm^2)	n_s (unitless)	χ^2
MB	SiO_2–NiO	1.17	1.87	0.48	1.58×10^{-3}
	SiO_2–MgO	1.20	0.51	0.97	1.77×10^{-3}
	SiO_2–$(Mg_{0.5}Ni_{0.5})O$	1.21	2.72	0.34	9.05×10^{-4}
AR27	SiO_2–NiO	0.13	0.54	0.31	4.80×10^{-4}
	SiO_2–MgO	0.016	0.37	0.53	9.13×10^{-4}
	SiO_2–$(Mg_{0.5}Ni_{0.5})O$	0.12	0.41	0.49	1.50×10^{-5}

		BET model parameters			
Model molecule	Nanoparticles	K_L (L nm^{-2})	K_U (L nm^{-2})	Q_m (molecules per nm^2)	χ^2
NR	SiO_2–NiO	0.90	0.08	9.33×10^{-2}	5.37×10^{-2}
	SiO_2–MgO	0.25	0.05	9.56×10^{-2}	4.77×10^{-2}
	SiO_2–$(Mg_{0.5}Ni_{0.5})O$	4.60	0.11	1.19×10^{-2}	5.09×10^{-2}

the surface than the Mg atoms in the prepared solid-mixture NiO–MgO, and thus, the low basicity was found for the SiO_2–$(Mg_{0.5}Ni_{0.5})O$ nanoparticles. This proposal seems to be reasonable by looking at the adsorption isotherm results (Fig. 7). We might conclude here that SiO_2–NiO nanoparticles are the best or the optimum adsorbents for all model molecules tested in this study. Although, SiO_2–$(Mg_{0.5}Ni_{0.5})O$ nanoparticles showed better adsorption performance with the cationic molecules (MB and NR), however, NiO seems to be the driving force of the synergistic effect of these nanoparticles rather than MgO. This could be attributed to the well-known stability of NiO nanoparticles in aqueous solutions.[77,78]

3.3 Model molecules adsorption followed by IR

Fig. 8 shows the infrared spectra of the silica-embedded NiO and/or MgO nanoparticles before and after adsorption. The signals of the framework regions (4000–2800 cm^{-1}) and (1800–400 cm^{-1}) of the prepared nanoparticles were clearly modified by signals corresponding to MB, NR, and AR27 upon their adsorption onto these nanoparticles. For instance, the IR modifications appear at 700–600 cm^{-1} (Fig. 8a) could be assigned to the C–S stretching vibration,[56] while IR signals at 3600 cm^{-1} (Fig. 8b) could be assigned to the asymmetrical stretching vibration of N–H bond, and signal appears at 1370 and 1247 cm^{-1} (Fig. 8c) might correspond to N=N stretching vibration[79] and to the $-SO_3-$ asymmetric stretching vibration, respectively. Interestingly, noticeable changes to the –OH stretching vibrations at around 3700–3400 cm^{-1} emerge significantly in the spectra of SiO_2–MgO and SiO_2–$(Mg_{0.5}Ni_{0.5})O$ nanoparticles, while it is not that significant for SiO_2–NiO nanoparticles. A reasonable explanation could be drawn here is that a partial hydration of MgO proceeded *via* water dissociation at the oxide surface, and thus, breakup of Mg^{2+}–O^{2-} surface elements, and their subsequent solvation led to form surface $Mg(OH)_2$ (ref. 80) which in our case seems to be affecting the adsorption of the model molecules onto MgO. Baumann *et al.*,[80] concluded that MgO nanoparticles, which were cubic in shape, dissolved with a significantly smaller dissolution rate in water when their size distribution is in the range 10–1000 nm. This confirms that the adsorption properties of nanoparticles do not depend only on the surface area but also related to the nanosize, nanocrystal shape, morphology, and polar surfaces.[30,31,80,81] Moreover, the intensity of these changes is slightly bigger in case of AR27 (Fig. 8c) at 3690 cm^{-1}, this could be attributed to the extra OH exists in the AR27 structure. Although, our prepared SiO_2–MgO nanoparticles succeeded in adsorbing the model molecules and the nano-MgO may be more stable when embedded in silica than when the nano-MgO is alone, however, their performance in the aqueous solutions was the worst. On the other hand, NiO nanoparticles are more stable in aqueous solutions;[77,78] thus, the formation of the hydroxylated surface is less prone to occur. This stability seems to be supported by the IR spectra (region 3700–3400 cm^{-1}) where no increase of hydroxyls occurred for SiO_2–NiO nanoparticles after the adsorption (Fig. 8). For the SiO_2–MgO and SiO_2–$(Mg_{0.5}Ni_{0.5})O$ clear IR band intensity changes on the –OH bending vibration mode are seen at around 1650–1370 cm^{-1}, in addition to IR band shifts with different intensities at around 1000–400 cm^{-1} indicating how the aqueous adsorption of the model molecules affected the IR vibration of the employed nanoadsorbents.

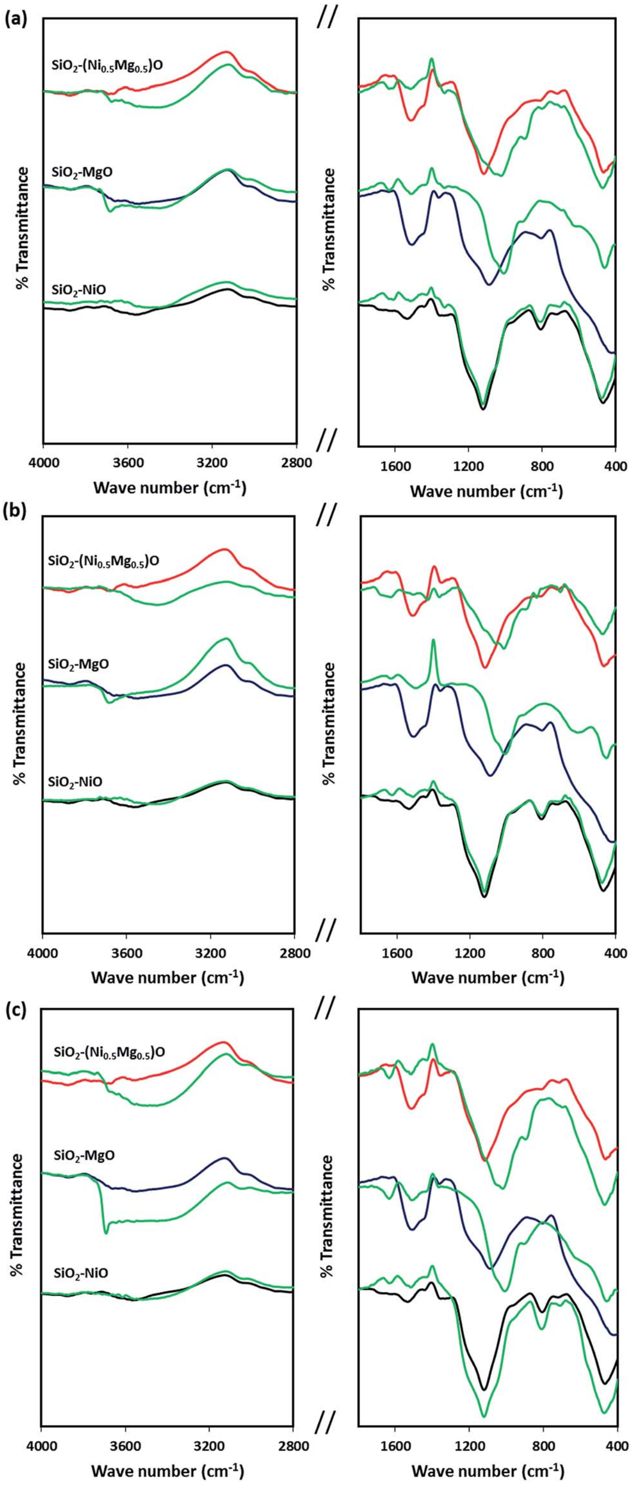

Fig. 8 Infrared spectra of silica-embedded NiO and/or MgO nanoparticles before and after adsorption of model molecules (a) MB, (b) NR, and (c) AR27 onto these nanoparticles (green spectra).

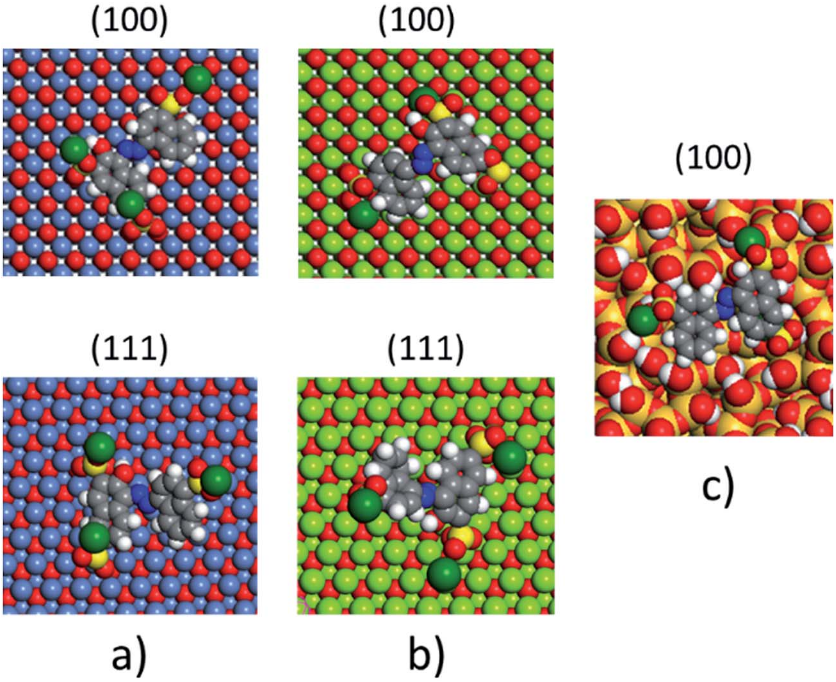

Fig. 9 CPK representation of the adsorbed AR27 molecule onto the (100) and (111) surfaces of: (a) NiO, (b) MgO, and (c) amorphous SiO_2. Grey atoms represent carbon, bright blue atoms represent nitrogen, white atoms represent hydrogen, yellow atoms represent sulfur, dark green atoms represent sodium, pale green atoms represent chlorine, bright green atoms represent magnesium, pale blue atoms represent nickel, dark yellow atoms represent silicon and red atoms represent oxygen.

3.4 Computational modeling results

The non-polar (100) surface is the most stable surface termination of the rock-salt type compounds being indeed the natural cleavage plane in this structure. This is due to the close packed bulk-like structure having equal amounts of anions and cations on each of these (100) planes.[82] On the other hand, the polar (111) surface is much less stable and it is known to

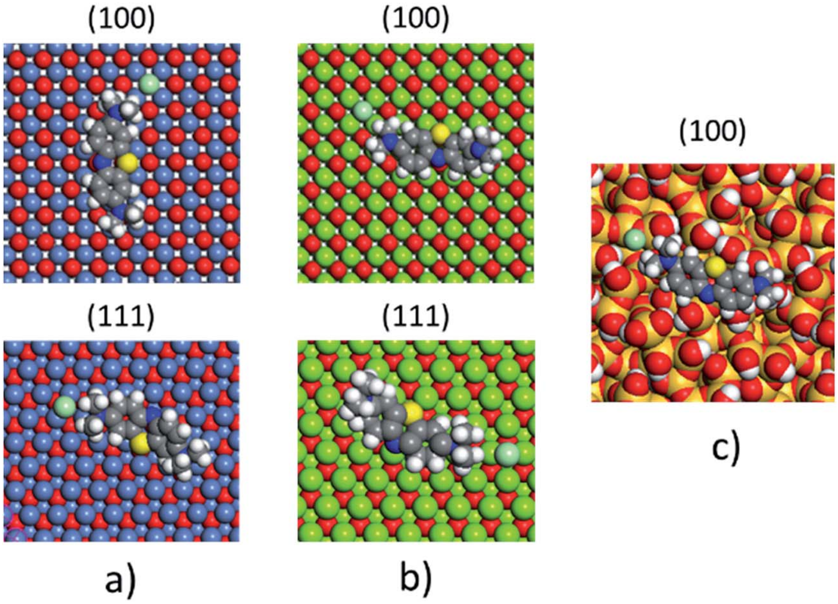

Fig. 10 CPK representation of the adsorbed MB molecule onto the (100) and (111) surfaces of: (a) NiO, (b) MgO, and (c) amorphous SiO_2. Grey atoms represent carbon, bright blue atoms represent nitrogen, white atoms represent hydrogen, yellow atoms represent sulfur, pale green atoms represent chlorine, bright green atoms represent magnesium, pale blue atoms represent nickel, dark yellow atoms represent silicon and red atoms represent oxygen.

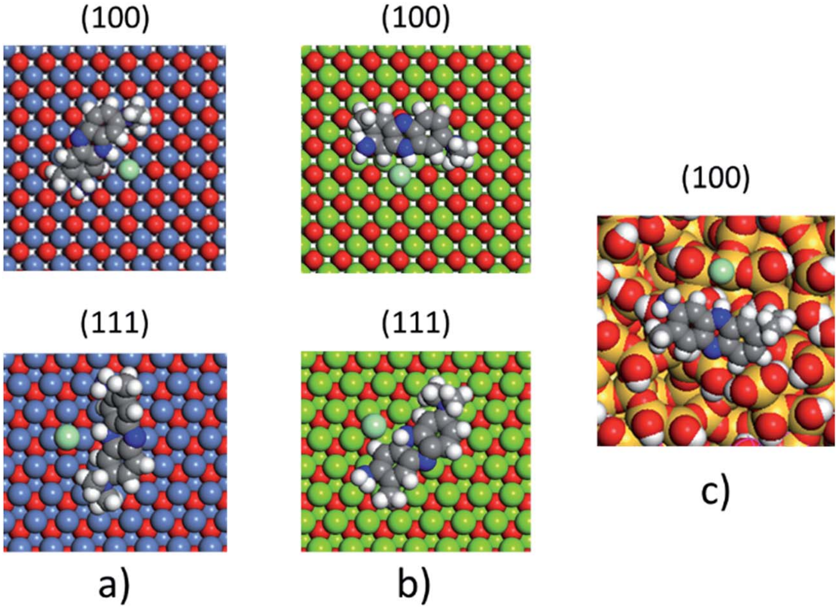

Fig. 11 CPK representation of the adsorbed NR molecule onto the (100) and (111) surfaces of: (a) NiO, (b) MgO, and (c) amorphous SiO_2. Grey atoms represent carbon, bright blue atoms represent nitrogen, white atoms represent hydrogen, pale green atoms represent chlorine, bright green atoms represent magnesium, pale blue atoms represent nickel, dark yellow atoms represent silicon and red atoms represent oxygen.

reconstruct to form different octopolar terminations with 2 × 2 periodicities (metal and oxygen terminated) to get stabilized.[83,84] However, in the presence of water, the (111) facet can be greatly stabilized by the hydroxylation of the surface.[85] Also, for the particular case of MgO, it has been found that nanocrystalline MgO can be dissolved fast in water if having sizes below 10 nm at pH $\geq$ 10.[80] On the contrary, if the size distribution is within the range of 10 to 1000 nm the crystals dissolve with a significantly smaller dissolution rate in water and the bigger the crystals the smaller the dissolution rate.[80] Thus, the previous information needs to be taken into account, for the samples with MgO, to understand the obtained experimental adsorption results. Calculations of the adsorption of AR27, MB, NR and water molecules onto the two surfaces of the oxides of nickel and magnesium were carried out to get some atomistic insight into the complex interaction of these molecules with the selected surfaces. Fig. 9–11 illustrate the adsorption of one molecule of AR27, MB or NR onto the (100) and (111) surfaces of NiO, MgO, and (100) amorphous SiO_2 surface, respectively.

As seen in these figures, in most of the cases, the adsorbed molecules tend to lay flat on the surface of the materials with the exception of the NR which in the (111) surfaces tend to be adsorbed slightly tilted when compared with the other ones. This may indicate that the configuration of the NR molecule will affect the adsorption of other NR molecules changing in this way the type of observed adsorption isotherm, as indeed was observed experimentally. The adsorption of the molecules on the surfaces was accomplished by interaction of the heteroatoms oxygen (AR27) and nitrogen (MB and NR) and the aromatic rings (all of them) with the exposed nickel and magnesium atoms on the surfaces. Table 6 shows a summary of the obtained adsorbed energies for each molecule on the different surfaces.

As can be inferred from the values in Table 6, AR27 is the organic molecule that has the strongest adsorption interaction with the different surfaces (more negative values for the adsorption energy) being the interaction with the surface (111) stronger than with the (100) surface for MgO which should be expected as this polar surface would be stabilized by strongly adsorbing the organic molecules. MB and NR also presented higher adsorption energies for the (111) surfaces; however, the interaction with the MgO is stronger than with the NiO surfaces; thus, without an aqueous media, MgO will adsorb the organic molecules stronger than NiO. As expected, the interactions of

Table 6 Adsorption energies for one AR27, MB, NR and H_2O molecule adsorbed on the studied surfaces having dimensions of ~3 nm × ~3 nm

	AR27 adsorption energy (kcal mol^{-1})		MB adsorption energy (kcal mol^{-1})		NR adsorption energy (kcal mol^{-1})		H_2O adsorption energy (kcal mol^{-1})	
Material	(100)	(111)	(100)	(111)	(100)	(111)	(100)	(111)
NiO	−2865	−2652	−1057	−2030	−992	−2042	−254	−208
MgO	−6295	−7238	−2411	−4999	−2298	−5055	−590	−544
SiO_2	−1090	—	−315	—	−338	—	−222	—

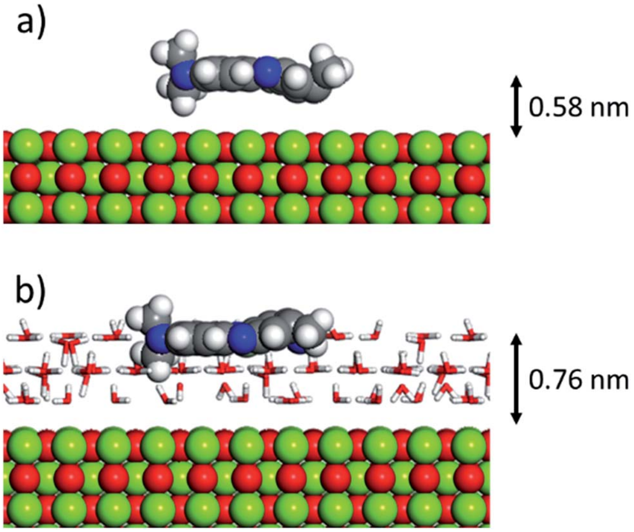

Fig. 12 CPK representation of the adsorbed NR molecule onto the MgO surface (100): (a) without water molecules (b) with 100 water molecules (represented as white and red sticks). Grey atoms represent carbon, bright blue atoms represent nitrogen, white atoms represent hydrogen, pale green atoms represent chlorine, bright green atoms represent magnesium, and red atoms represent oxygen.

these molecules with the amorphous silica surface are the lowest; thus, the nanocrystalline oxides are the ones driving the adsorption process and the amorphous silica is simply a carrier for maintaining nanoparticles stability. Interestingly, the adsorption of water onto the surfaces of NiO and MgO indicates that adsorption of water on the MgO surfaces is stronger; thus, this behavior of water should affect the adsorption of the organic molecules on the MgO surfaces under the aqueous system. Fig. 12 shows the adsorption of NR on the surface (100) of MgO without the presence of water molecules (Fig. 12a) and in the presence of 100 molecules of water (Fig. 12b). The presence of water seems to have weakened the interaction of NR with the surface and the interatomic adsorption distance of NR from the surface increased from 0.58 nm to 0.76 nm when the water molecules are present. This strongly suggests that the water will influence the adsorption of the organic molecules on the MgO surfaces as experimentally observed. The adsorption of water on the surfaces of MgO is of the chemisorption type; thus, hydroxylation of the surfaces will change the way the organic molecules will interact with the surfaces, and experimentally it seemed that the adsorption was weakened.

Electron density distribution is a key descriptor for molecular systems because it influences intersystem interactions due to electrostatic or electrodynamic phenomena; thus, calculations of this key descriptor were carried out to further get insights into the observed behavior of the selected organic molecules. Fig. 13 shows the DFT optimized AR27, MB, and NR organic molecules with their electrostatic potential maps computed at the DFT m-GGA-M06L/DNP+ level using the COSMO water solvation model. The red color in the maps indicates a more negative region and the positive zones are presented as blue surfaces. Fig. 13 clearly depicts that the three organic model molecules have undeniable different charge distributions; and thus, should have completely different behaviors under the tested adsorption conditions implying the need for a molecular level description of their behaviors. As can be noticed in Fig. 13a and b, the sulfur atoms, in the sulfonate groups of AR27, are surrounded by oxygen atoms rendering this group as a hard anion chemical species, thus, the negative charge is quite localized in AR27 within the sulfonate groups; and then, coulombic and hydrophobic/hydrophilic forces should dictate its physicochemical behavior. On the other hand, the NR molecule features a finer structure with locally negative and positive zones distributed along the molecule. This distribution of negative and positive charges may explain the observed BET adsorption behavior for this molecule as the adsorbed NR molecule can act as a new sorption site for new NR molecules as the environmental charges may render this molecule to act like "bricks", thus, each will be piling up on top of the previous one generating the BET type model adsorption behavior that was observed experimentally. Finally, for the MB molecule case, the positives zones are less localized than in the case of the NR molecule, and thus, the behavior of this molecule

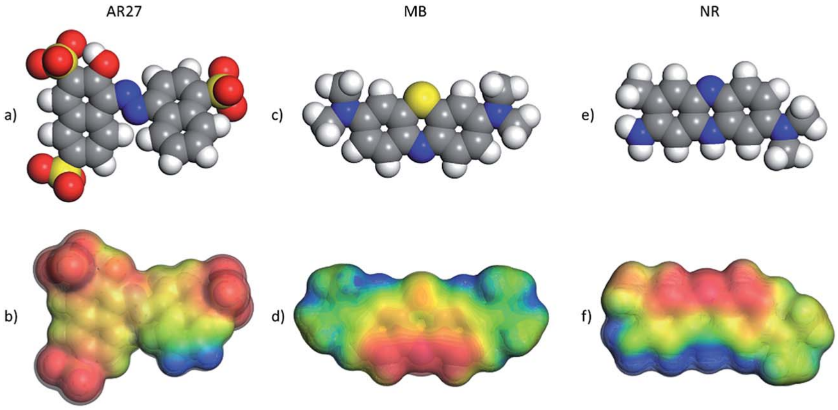

Fig. 13 Geometrically optimized organic molecules (top) and their electrostatic potential maps (bottom) computed at the DFT m-GGA-M06-L/DNP+ level with the COSMO water solvation model. Red surfaces enclose a negative charge, while positive zones are presented as blue surfaces.

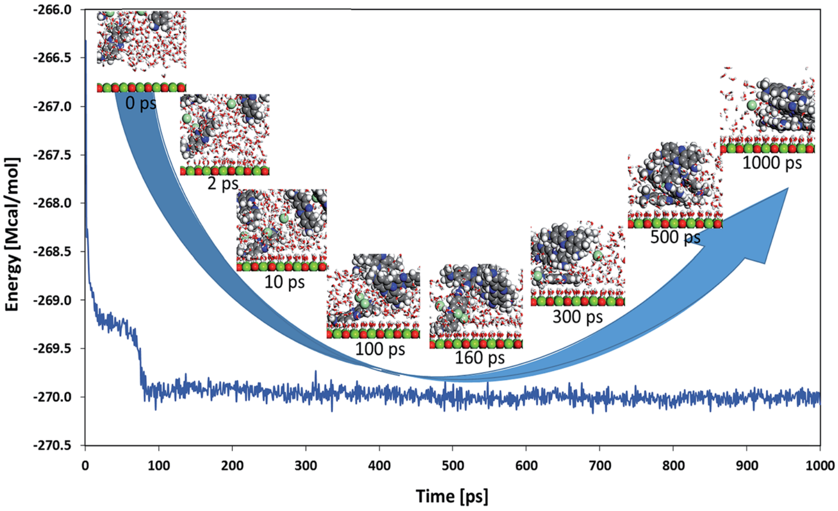

Fig. 14 Total energy as a function of simulation time for the system comprising the (100) surface of MgO, 5 NR molecules, and 500 water molecules. In the insets, the NR molecules and MgO surface are represented as spheres and water molecules are represented as sticks: grey atoms represent carbon, bright blue atoms represent nitrogen, white atoms represent hydrogen, pale green atoms represent chlorine, bright green atoms represent magnesium, and red atoms represent oxygen.

is different from the NR one but more similar to the AR27 molecule producing adsorption behavior that complies with the Sips model.

A molecular dynamics simulation was carried out with five NR molecules together with 500 water molecules on top of the (100) surface of MgO to get some additional insights into the adsorption behavior of this system. Fig. 14 shows the total energy of the system as a function of simulation time with insets of the close-up evolution of the system with selected simulation times (to get finer details of the process, a video of the evolution of the system can be found in the accompanying ESI†). An important drop of the total energy for the system was obtained when some water molecules got adsorbed on the surface and one of the NR molecules got also adsorbed on the surface (approximately between 0 and 10 ps of simulation time). A second drop of the total energy was observed when the remaining four NR molecules got together forming a 4-molecule cluster (approximately between 10 and 100 ps of simulation time). Finally, the system entered in equilibrium (maintaining the total energy around -270 Mcal mol^{-1}) when the four NR molecules non-adsorbed on the surface interacted with the one that was adsorbed on the surface making a cluster of 5 NR molecules which now act together by moving and vibrating on the surface; one of them directly adsorbed on the surface and the others forming a cluster adsorbed on top of the first one. This finding seems to give a feasible explanation for the observed BET type adsorption behavior encountered with the NR model molecule on the studied silica-embedded NiO and MgO nanoparticles in the experimental part.

4. Conclusions

Different silica-embedded NiO and/or MgO nanoparticles (SiO_2–NiO, SiO_2–MgO, and SiO_2–($Ni_{0.5}Mg_{0.5}$)O) were synthesized and characterized by different characterization techniques like XRD, BET, HRTEM, CO_2-TPD, and IR spectroscopy. These nanoparticles were successfully employed for the adsorptive removal of different cationic and anionic model organic molecules, exemplified by methylene blue (MB), neutral red (NR), and acid red 27 (AR27). On a normalized surface area basis, SiO_2–($Ni_{0.5}Mg_{0.5}$)O nanoparticles showed the highest uptake for MB and NR which could be attributed to their possible synergistic effect, while SiO_2–NiO nanoparticles showed the highest uptake for AR27 which could be attributed to the stability of NiO nanoparticles in comparison with MgO in aqueous solutions as the adsorption of water onto the surface of MgO is stronger. These findings were supported by the IR spectroscopy before and after adsorption. The experimental adsorption macroscopic isotherm data for MB and AR27 fit well with the Sips model with a heterogeneity factor of less than 0.5 in most cases suggesting that these nanoparticles may have heterogeneous surfaces with adsorption sites that have different adsorption energies. Unexpectedly, the adsorbed amount of NR molecules increased exponentially with the equilibrium concentration. Thus, data fit well to the BET model suggesting a multilayer adsorption system. These findings were confirmed and supported by the computational modeling, DFT calculations, and molecular dynamics simulation. MB and AR27 model molecules tended to lay flat on the surface of the nanoparticles while NR tended to be adsorbed slightly tilted. The adsorption of the molecules on the surfaces was accomplished by interaction of the heteroatoms and the aromatic rings with the exposed nickel and magnesium atoms on the surfaces. The molecular dynamics simulation movie together with the evolved total adsorption energy as a function of simulation time confirmed the experimental BET adsorption behavior of NR onto the prepared nanoparticles. We do believe that the development of such simple and cost-effective silica-embedded NiO and/or

MgO nanoparticles will be promising for the futuristic steam gasification of the adsorbed species, and thus, working not only as nanoadsorbents but also as nanocatalysts. After understanding the adsorption mechanism of tested model molecules in this study, the catalytic behavior of these nanoparticles will be addressed in future publications.

Acknowledgements

The authors are grateful to the Department of Chemical and Petroleum Engineering at the Schulich School of Engineering at the University of Calgary. The prestigious Werner Graupe International Fellowship in Engineering hosted by the University of Calgary is deeply appreciated. A special thanks to Dr Azfar Hassan for thorough elaborations on the CO_2-TPD test, and Dr Tobias Fürstenhaupt for access to the Microscopy and Imaging Facility of the Health Science Center at the University of Calgary which receives support from the Canadian Foundation for Innovation and the Alberta Science and Research Authority.

References

1 L. M. L. Nollet and L. S. P. D. Gelder, *Handbook of water analysis*, Taylor & Francis Group, LLC, Boca Raton, FL, 3rd edn, 2014.
2 F. S. G. Einschlag and L. Carlos, *Waste water – treatment technologies and recent analytical developments*, InTech, Rijeka, 2013.
3 D. Barceló and M. Petrovic, *Waste water treatment and reuse in the mediterranean region*, Springer, Verlag, Berlin, Heidelberg, 2011.
4 P. Martinez-Santos, M. M. Aldaya and M. R. Llamas, in *Integrated water resources management in the 21st century revisiting the paradigm*, ed. P. Martinez-Santos, M. M. Aldaya and M. R. Llamas, CRC Press Taylor & Francis Group, London, UK, 2014, ch. 2, pp. 17–36.
5 E. W. Allen, *J. Environ. Eng. Sci.*, 2008, **7**, 123–138.
6 E. W. Allen, *J. Environ. Eng. Sci.*, 2008, **7**, 499–524.
7 E. T. Igunnu and G. Z. Chen, *Int. J. Low-Carbon Technol.*, 2014, **9**, 157–177.
8 X. Qu, P. J. J. Alvarez and Q. Li, *Water Res.*, 2013, **47**, 3931–3946.
9 J. M. Perez, *Nat. Nanotechnol.*, 2007, **2**, 535–536.
10 K. J. McDonald, B. Reynolds and K. J. Reddy, *Sci. Rep.*, 2015, **5**, 11110.
11 F. Brandl, N. Bertrand, E. M. Lima and R. Langer, *Nat. Commun.*, 2015, 7765.
12 Y. Su, A. S. Adeleye, Y. Huang, X. Zhou, A. A. Keller and Y. Zhang, *Sci. Rep.*, 2016, **6**, 24358.
13 P. Westerhoff, P. Alvarez, Q. Li, J. Gardea-Torresdey and J. Zimmerman, *Environ. Sci.: Nano*, 2016, **3**, 1241–1253.
14 N. N. Nassar and A. Ringsred, *Environ. Eng. Sci.*, 2012, **29**, 790–797.
15 N. N. Nassar, N. N. Marei, G. Vitale and L. A. Arar, *Can. J. Chem. Eng.*, 2015, **93**, 1965–1974.
16 N. N. Nassar, in *Applications of nanomaterials for water quality*, ed. B. V. d. Bruggen, Future Science, London, 2013, pp. 52–65.
17 N. N. Nassar, in *Application of adsorbents for water pollution control*, ed. A. Bahtnagar, Bentham Science Publishers, 2012, pp. 81–118.
18 H. P. Jarvie and S. M. King, *Nano Today*, 2010, **5**, 248–250.
19 L. Zhang and M. Fang, *Nano Today*, 2010, **5**, 128–142.
20 P. Xu, G. M. Zeng, D. L. Huang, C. L. Feng, S. Hu, M. H. Zhao, C. Lai, Z. Wei, C. Huang, G. X. Xie and Z. F. Liu, *Sci. Total Environ.*, 2012, **424**, 1–10.
21 Y. Yuan, N. Yan and P. J. Dyson, *ACS Catal.*, 2012, **2**, 1057–1069.
22 D. Astruc, F. Lu and J. R. Aranzaes, *Angew. Chem., Int. Ed.*, 2005, **44**, 7852–7872.
23 N. Yan, C. Xiao and Y. Kou, *Coord. Chem. Rev.*, 2010, **254**, 1179–1218.
24 A. El-Qanni, N. N. Nassar, G. Vitale and A. Hassan, *J. Colloid Interface Sci.*, 2016, **461**, 396–408.
25 Q.-Y. Chen, D.-l. Huang, Y.-B. Wang, J. Shao and L.-L. Qu, *RSC Adv.*, 2016, **6**, 70547–70552.
26 N. Yan, *Nanotechnol. Rev.*, 2013, **2**, 485–486.
27 J. Singh, J.-K. Yang, Y.-Y. Chang and J. R. Koduru, *Environ. Processes*, 2016, 1–14, DOI: 10.1007/s40710-016-0199-2.
28 M. Santos-Beltrán, F. Paraguay-Delgado, R. García, W. Antúnez-Flores, C. Ornelas-Gutiérrez and A. Santos-Beltrán, *J. Mater. Sci.: Mater. Electron.*, 2016, 1–14, DOI: 10.1007/s10854-016-5878-2.
29 *JADE, V 7.5.1 XRD, Pattern Processing Identification & Quantification*, 2005.
30 N. N. Marei, N. N. Nassar and G. Vitale, *Phys. Chem. Chem. Phys.*, 2016, **18**, 6839–6849.
31 M. Hmoudah, N. N. Nassar, G. Vitale and A. El-Qanni, *RSC Adv.*, 2016, **6**, 64482–64493.
32 R. Sips, *J. Chem. Phys.*, 1948, **16**, 490–495.
33 R. Sips, *J. Chem. Phys.*, 1950, **18**, 1024–1026.
34 S. Brunauer, P. H. Emmett and E. Teller, *J. Am. Chem. Soc.*, 1938, **60**, 309–319.
35 D. C. Montgomery and G. C. Runger, *Applied statistics and probability for engineers*, John Wiley & Sons, New York, 4th edn, 2006.
36 *BIOVIA Materials Studio Modeling and Simulation Software Version 2017*, Dassault Systemes, accessed 8 November, 2016.
37 S. Kirkpatrick, C. D. Gelatt and M. P. Vecchi, *Science*, 1983, **220**, 671–680.
38 V. Černý, *J. Optim. Theor. Appl.*, 1985, **45**, 41–51.
39 L. Zhao, L. Liu and H. Sun, *J. Phys. Chem. C*, 2007, **111**, 10610–10617.
40 H. Sun, *J. Phys. Chem. B*, 1998, **102**, 7338–7364.
41 H. Sun and D. Rigby, *Spectrochim. Acta, Part A*, 1997, **53**, 1301–1323.
42 D. Rigby, H. Sun and B. E. Eichinger, *Polym. Int.*, 1997, **44**, 311–330.
43 H. Sun, P. Ren and J. R. Fried, *Comput. Theor. Polym. Sci.*, 1998, **8**, 229–246.

44 S. W. Bunte and H. Sun, *J. Phys. Chem. B*, 2000, **104**, 2477–2489.

45 M. J. McQuaid, H. Sun and D. Rigby, *J. Comput. Chem.*, 2004, **25**, 61–71.

46 A. Klamt and G. Schuurmann, *J. Chem. Soc., Perkin Trans. 2*, 1993, 799–805, DOI: 10.1039/p29930000799.

47 F. L. Hirshfeld, *Theor. Chim. Acta*, 1977, **44**, 129–138.

48 S. Nosé, *J. Chem. Phys.*, 1984, **81**, 511–519.

49 K. S. W. Sing, D. H. Everett, R. A. W. Haul, L. Moscou, R. A. Pieroti, J. Rouquerol and T. Siemieniewska, *Pure Appl. Chem.*, 1985, **57**, 603–619.

50 M. Thommes, K. Kaneko, A. V. Neimark, J. P. Olivier, F. Rodriguez-Reinoso, J. Rouquerol and K. S. W. Sing, *Pure Appl. Chem.*, 2015, **87**, 1051–1069.

51 N. N. Nassar, A. Hassan and P. Pereira-Almao, *Energy Fuels*, 2011, **25**, 1017–1023.

52 I. H. Chowdhury, A. H. Chowdhury, P. Bose, S. Mandal and M. K. Naskar, *RSC Adv.*, 2016, **6**, 6038–6047.

53 E. Roduner, *Chem. Soc. Rev.*, 2006, **35**, 583–592.

54 M. A. Peck and M. A. Langell, *Chem. Mater.*, 2012, **24**, 4483–4490.

55 S. Musi, N. Filipovi-Vincekovi and L. Sekovani, *Braz. J. Chem. Eng.*, 2011, **28**, 89–94.

56 R. M. Silverstein, F. X. Webster and D. J. Keimle, *Spectrometric identification of organic compounds*, John Wiley & Sons, NJ, USA, 7th edn, 2005.

57 K. Scherer, L. Nouvelot, P. Lacan and R. Bosmans, *Appl. Opt.*, 1996, **35**, 5067–5072.

58 J. K. Sharma, P. Srivastava, G. Singh, M. S. Akhtar and S. Ameen, *Ceram. Int.*, 2015, **41**, 1573–1578.

59 L. Liu, Y. Guo, Y. Wang, X. Yang, S. Wang and H. Guo, *Electrochim. Acta*, 2013, **114**, 42–47.

60 L.-X. Li, D. Xu, X.-Q. Li, W.-C. Liu and Y. Jia, *New J. Chem.*, 2014, **38**, 5445–5452.

61 N. N. Nassar, C. A. Franco, T. Montoya, F. B. Cortés and A. Hassan, *Fuel*, 2015, **156**, 110–120.

62 C. A. Franco, T. Montoya, N. N. Nassar, P. Pereira-Almao and F. B. Cortés, *Energy Fuels*, 2013, **27**, 7336–7347.

63 C. A. Franco, N. N. Nassar, T. Montoya and F. B. Cortés, in *Handbook on Oil Production Research*, ed. J. Ambrosio, Nova Science Publishers Inc., USA, 2014.

64 R. Li, L. Zhang and P. Wang, *Nanoscale*, 2015, **7**, 17167–17194.

65 C. C. Acebal, B. M. Simonet and M. Valcárcel, *TrAC, Trends Anal. Chem.*, 2013, **43**, 109–120.

66 C.-H. Huang, K.-P. Chang, H.-D. Ou, Y.-C. Chiang, E. E. Chang and C.-F. Wang, *J. Hazard. Mater.*, 2011, **186**, 1174–1182.

67 R. Wu, J.-H. Liu, L. Zhao, X. Zhang, J. Xie, B. Yu, X. Ma, S.-T. Yang, H. Wang and Y. Liu, *J. Environ. Chem. Eng.*, 2014, **2**, 907–913.

68 W. Fan, W. Gao, C. Zhang, W. W. Tjiu, J. Pan and T. Liu, *J. Mater. Chem.*, 2012, **22**, 25108–25115.

69 K. Y. Foo and B. H. Hameed, *Chem. Eng. J.*, 2010, **156**, 2–10.

70 M. Choimet, A. Tourrette and C. Drouet, *J. Colloid Interface Sci.*, 2015, **456**, 132–137.

71 A. Ebadi, J. S. Soltan Mohammadzadeh and A. Khudiev, *Adsorption*, 2009, **15**, 65–73.

72 J. Wang, C. P. Huang, H. E. Allen, D. K. Cha and D.-W. Kim, *J. Colloid Interface Sci.*, 1998, **208**, 518–528.

73 N. N. Nassar, L. A. Arar, N. N. Marei, M. M. Abu Ghanim, M. S. Dwekat and S. H. Sawalha, *Environmental Nanotechnology, Monitoring & Management*, 2014, **1–2**, 14–23.

74 C. A. Franco, N. N. Nassar and F. B. Cortés, *J. Colloid Interface Sci.*, 2014, **433**, 58–67.

75 C.-H. Weng and Y.-F. Pan, *J. Hazard. Mater.*, 2007, **144**, 355–362.

76 C.-H. Weng and Y.-F. Pan, *Colloids Surf., A*, 2006, **274**, 154–162.

77 Y. Zhang, Y. Chen, P. Westerhoff, K. Hristovski and J. C. Crittenden, *Water Res.*, 2008, **42**, 2204–2212.

78 Y. Zhang, Y. Chen, P. Westerhoff and J. Crittenden, *Water Res.*, 2009, **43**, 4249–4257.

79 N. N. Nassar, *Sep. Sci. Technol.*, 2010, **45**, 1092–1103.

80 S. O. Baumann, J. Schneider, A. Sternig, D. Thomele, S. Stankic, T. Berger, H. Grönbeck and O. Diwald, *Langmuir*, 2015, **31**, 2770–2776.

81 E. Lucas, S. Decker, A. Khaleel, A. Seitz, S. Fultz, A. Ponce, W. Li, C. Carnes and K. J. Klabunde, *Chem.–Eur. J.*, 2001, **7**, 2505–2510.

82 P. W. Tasker, *J. Phys. C: Solid State Phys.*, 1979, **12**, 4977.

83 D. Wolf, *Phys. Rev. Lett.*, 1992, **68**, 3315–3318.

84 D. Wolf, *Solid State Ionics*, 1995, **75**, 3–11.

85 J. Ciston, A. Subramanian and L. D. Marks, *Phys. Rev. B: Condens. Matter Mater. Phys.*, 2009, **79**, 085421.